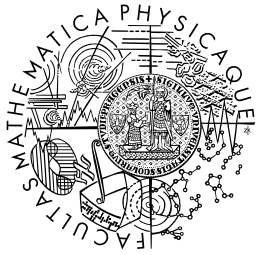

FACULTY
OF MATHEMATICS
AND PHYSICS
Charles University

BACHELOR THESIS

Kateřina Rezková

Application of Lagrangian coherent structures to the stratospheric winter polar circulation

Department of Atmospheric Physics

Supervisor of the bachelor thesis: Prof. RNDr. Petr Pišoft, Ph.D.
Study programme: Physics
Study branch: Physics

Prague 2024

I declare that I carried out this master thesis independently, and only with the cited sources, literature and other professional sources. It has not been used to obtain another or the same degree.

I understand that my work relates to the rights and obligations under the Act No. 121/2000 Sb., the Copyright Act, as amended, in particular the fact that the Charles University has the right to conclude a license agreement on the use of this work as a school work pursuant to Section 60 subsection 1 of the Copyright Act.

In ..... date ....

Author's signature

I would like to thank my supervisor, Prof. RNDr. Petr Pišoft, Ph.D., for introducing me to the fascinating topic of Lagrangian coherent structures and their role in fluid dynamics, and also for his helpful remarks regarding the structure of this thesis. A special thank you goes to my parents and my sister, for always encouraging me on my academic journey and believing in my perseverance. Lastly, I thank all my friends and colleagues who helped me keep motivated throughout the process of writing this thesis.

Title: Application of Lagrangian coherent structures to the stratospheric winter polar circulation

Author: Kateřina Rezková

Department: Department of Atmospheric Physics

Supervisor: Prof. RNDr. Petr Pišoft, Ph.D., Department of Atmospheric Physics

Abstract: The objective of this thesis is to introduce the theory of Lagrangian coherent structures (LCSs) and analyze LCSs on atmospheric data. Specifically, the focus is on the stratospheric winter polar circulation on the Northern Hemisphere. Computations were performed using the Python programming language with the main obstacle of the computations being singularity at the North Pole. The time period studied was December 2007 to February 2008. Hyperbolic LCSs were calculated for this specific time frame and subsequently studied and analysed. Three main events in the evolution of the polar vortex were described: the formation, the stabilisation and the collapse of the vortex.

Keywords: Lagrangian coherent structures, LCSs, Polar vortex, Stratosphere

Název práce: Aplikace Lagrangeových koherentních struktur na stratosférickou zimní polární cirkulaci

Author: Kateřina Rezková

Katedra: Katedra fyziky atmosféry

Vedoucí práce: Prof. RNDr. Petr Pišoft, Ph.D., Katedra fyziky atmosféry

Abstrakt: Cílem této práce je představit teorii Lagrangeových koherentních struktur (LCSs) a analyzovat LCSs na atmosférických datech. Konkrétní zaměření je na stratosférickou zimní polární cirkulaci na severní polokouli. Výpočty byly prováděny pomocí programovacího jazyka Python, přičemž hlavní překážkou výpočtů byla singularita na severním pólu. Studované časové období bylo prosinec 2007 až únor 2008. Hyperbolické LCSs byly vypočteny pro tento konkrétní časový rámec a následně studovány a analyzovány. Byly popsány tři hlavní události ve vývoji polárního víru: vznik, stabilizace a kolaps víru.

Klíčová slova: Lagrangeovy koherentní struktury, LCSs, Polární vír, Stratosféra

List of Symbols

t_0	initial time
t	time
$\mathbf{x}_0(t)$	initial position
$\mathbf{x}\left(t; t_0, \mathbf{x}_0\right)$	trajectory
$\dot{\mathbf{x}}$	time derivative of $\mathbf{x}$
$\mathbf{v}(\mathbf{x}, t)$	velocity field
$\mathbf{F}_{t_0}^{t}\left(\mathbf{x}_0\right)$	flowmap
∇	gradient
$\nabla\mathbf{F}_{t_0}^{t}\left(\mathbf{x}_0\right)$	deformation gradient
$\mathbf{C}_{t_0}^{t}\left(\mathbf{x}_0\right)$	right CG strain tensor
$\mathbf{B}_{t_0}^{t}\left(\mathbf{x}_0\right)$	left CG strain tensor
$\mathcal{M}(t)$	material surface
$\boldsymbol{\xi}(t)$	material perturbance
$\boldsymbol{\xi}_i$	eigenvector
λ_i	eigenvalue

List of Abbreviations

CG tensor	right Cauchy-Green strain tensor
FTLE	finite-time Lyapunov exponent
IC	initial condition
LCS	Lagrangian coherent structure
NH	northern hemisphere
PV	potential vorticity
RK4	Runge-Kutta method
SH	southern hemisphere
SSW	sudden stratospheric warming
UV	ultraviolet

Contents

Introduction

Scientist have always been subjected to the uneasy task to mathematically describe and model fluid dynamics. Real flows often exhibit chaotic behaviour that is difficult to predict. An especially intriguing challenge in the world of hydrodynamics is determining the location of transport barriers. These curves serve as boundaries of flow over a specified period of time. There are two approaches used for modelling the evolution of continuum. The Eulerian and the Lagrangian method. The Eulerian approach has been preferred in the past. It focuses on a velocity field rather than on material trajectories. Lately, new Lagrangian methods have been developed. These methods, which are derived from the trajectories a fluid parcel follows, have proved to be much more accurate than the outdated Eulerian methods [Haller, 2023]. In this thesis, we focus on a method called Lagrangian coherent structures.

Lagrangian coherent structures (LCSs) is a method first introduced in 2000 by George Haller and Guo-Cheng Yuan (Haller and Yuan [2000]). They developed an elegant mechanism that utilizes Cauchy-Green strain tensor, its eigenvalues and eigenvectors and finite-time Lyapunov exponents (FTLEs). Ridges of maximal FTLEs values can be interpreted as transport barriers. In this thesis, we will apply a specific type of LCSs called hyperbolic LCSs. They represent transport barriers that are either most repelling or most attracting. It is the repelling hyperbolic LCSs that become significant when determining the edge of a polar vortex.

Stratospheric polar winter circulation, often referred to as simply the "polar vortex", is a rotating mass of air in the upper atmosphere, forming every year at the beginning of winter months. It is present around both the North and the South Pole. Both vortices have their specific properties and they are generally of different significance. The Antarctic polar vortex is largely linked to the ozone hole, a phenomenon that has huge impacts on our population, leading to health risks and even the development of skin cancer [Zhang et al., 2017]. The Arctic polar vortex is important regarding winter surface weather, as its collapse leads to extreme weather events, impacting North America, northern Europe and Asia. This incident is called sudden stratospheric warming [Waugh et al., 2017]. The focus of this thesis is on the polar vortex located on the Northern Hemisphere.

The ability to predict the breakdown of the polar vortex would lead to improvements in forecasts of extreme weather events. For its great impact on the surface weather, there have been many attempts to successfully detect the edge of the polar vortex and trace its changes. The LCS-method has the potential to be a more exact and more accurate method than any other approach introduced up to date. In this thesis, we will attempt to demonstrate this method on atmospheric data for the winter of 2007/2008 and analyse our results in the hopes of detecting the edge of the polar vortex and its evolution.

1. Fluid dynamics and LCSs

A relatively new method, first introduced by Haller and Yuan in 2000 called the *Lagrangian coherent structures* (LCSs) allows for deeper study of fluid dynamical systems. Its charm and significance lies within the usage of the Lagranginan approach rather than the Eulerian approach. Lagrangian approach focuses on material surfaces, following all material points and their evolution in time, as opposed to the Eulerian approach which works with velocity fields. A grand advantage of the Lagrangian methods is that they can (with great accuracy) not only trace back, but also predict the movement of a mass in space [Haller, 2023].

The aim of this chapter is to bring closer the fundamentals of fluid dynamics in the Lagrangian language and introduce the computation of LCSs. Before we begin, let us first define the LCSs as in Haller [2023]: "Lagrangian coherent structures (LCSs) are codimension-1, structurally stable material surfaces that locally extremize attraction, repulsion or shear among all nearby material surfaces over a finite time interval $[t_0; t_1]$".

1.1 Transport barriers

In fluid dynamics, the term *transport barrier* is self-explanatory; it represents an inhibitor of flow. It is substantially important, nevertheless not necessarily straightforward to define those barriers precisely. The endeavor to mathematically specify transport barriers yields different approaches, where one of them (and a fairly succesful one) is the LCSs method. Especially in geophysical flows studied in atmospheric and oceanic physics, detecting transport barriers plays a crucial role. Observable transport barrier can be seen in Figure 1.1. An oil spill in the Gulf of Mexico creates coherent structures visible due to the difference of colour between blue water and red oil [Haller, 2023].

Given initial conditions (ICs), it is often important to define surfaces which correctly follow evolution in time. Chaotic theory tells us that even the slightest perturbations between separate individual sests of initial conditions can lead to vast disparities. As a result, mathematical models can be assessed in terms of

Figure 1.1: Oil spill in the Gulf of Mexico. Distinctive transport barriers are apparent, highlighted with strong colour differences. [Haller, 2023]

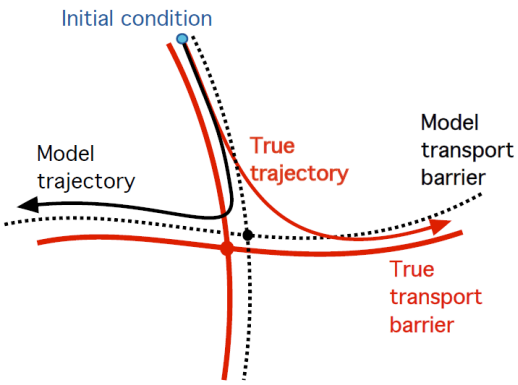

Figure 1.2: True and model trajectory and transport barrier. Model trajectory (black) does not correspond with true trajectory (red). Model transport barrier (red) corresponds well with true transport barrier (red). [Haller, 2023]

their ability to correctly reconstruct transport barriers. An example is seen in Figure 1.2. The model provided does not yield correct trajectories, however, the construction of model transport barrier corresponds very well. Smooth surfaces that can block transport locally must be *codimension-1* invariant manifolds. That is, they must exist in 2-dimensional flows and surfaces in 3-dimensional flows. Only then can they be defined as transport barriers [Haller, 2023].

Idealized transport barriers for advective transport are manifolds of a saddle point for all times, visualisation is seen in Figure 1.3. Let us have a fluid parcel that is being carried by advection. It follows the trajectory of a stable manifold. As it approaches the saddle point, it will be diverted along the unstable manifold (red). Further in this thesis we discover that the stable manifold can be computed as an attracting LCS and the unstable manifold as a repelling LCS [Peacock and Haller, 2013].

In reality, it is often desired to study an area set in a specific finite continuous time interval. The continuity of time introduces additional problems, as the uniqueness of material surfaces is lost, the reason being the fact that many similar trajectories could be classified as transport barriers (*material surface* is a manifold of material particles that evolve in time given ICs). To resolve this discrepancy, we study only *coherent* surfaces. Coherent surfaces are resilient structures that keep their spatial integrity over a specified time interval [Haller, 2023].

1.2 Description of Lagrangian flow

In fluid dynamics, there are two approaches used to describe flow. Let us consider an at least continuously differentiable velocity field

$$\dot{\mathbf{x}} = \mathbf{v}(\mathbf{x}, t). \tag{1.1}$$

In practice, the velocity field is either given or numerically computed from data (see Section 3.4). A *flowmap* is a function denoting the evolution of a trajectory given its initial position $\mathbf{x_0}$. It can be defined as follows:

$$\mathbf{F}_{t_0}^{t} : \mathbf{x}_0 \mapsto \mathbf{x}\left(t; t_0, \mathbf{x}_0\right). \tag{1.2}$$

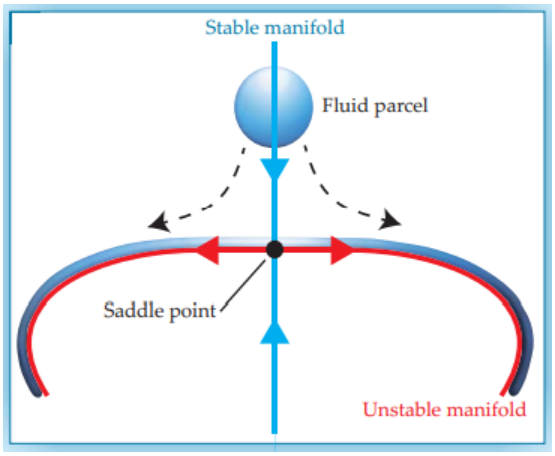

Figure 1.3: Behaviour of a fluid parcel near saddle point. Fluid parcel (blue) approaches a saddle point (black) and an unstable manifold (red), following a stable manifold (blue). [Peacock and Haller, 2013]

This is called the *Lagrangian description*, which focuses on tracing the evolution of a *flow tracer* (a chosen material point, typically a dye or a smoke particle) from an initial position in time and space. In other words, the Lagrangian method finds the trajectories of flow tracers, typically used for advection. The *Eulerian description* is often used when describing deformations, as it follows the evolution of the Eulerian vector field [Boffetta et al., 2001].

Tracers can be active or passive. Passive tracers are simply being carried by the Eulerian velocity field, not otherwise interacting or impacting the original flow. Active tracers, on the other hand, can have an effect on the field. A typical active tracer is vorticity or kinetic energy [Haller, 2023].

If we take the gradient of the flowmap, we obtain a *deformation gradient* $\nabla \mathbf{F}_{t_0}^{t}(\mathbf{x}_0)$. Since we consider an at least continuously differentiable velocity field, the flowmap is a *diffeomorphism*, meaning its inverse is also its transpose. Clearly,

$$\mathbf{F}_{t_0}^{t}\left(\mathbf{F}_{t}^{t_0}(\mathbf{x})\right) = \mathbf{x}. \tag{1.3}$$

The deformation gradient is a mapping between two different tangent spaces. As a result, it does not have a clearly defined eigenvalues and eigenvectors. A *Lagrangian tensor* is a linear mapping from tangent spaces to themselves. The deformation gradient is therefore not a Lagrangian tensor. However, using the noted definition and the fact that the deformation gradient is a mapping between tangent spaces, we can define the *right Cauchy-Green strain tensor (CG tensor)* as follows:

$$\mathbf{C}_{t_0}^{t}(\mathbf{x}_0) = \left[\nabla \mathbf{F}_{t_0}^{t}(\mathbf{x}_0)\right]^{\mathrm{T}} \nabla \mathbf{F}_{t_0}^{t}(\mathbf{x}_0). \tag{1.4}$$

Clearly, the CG tensor is an example of a Lagrangian tensor. It can read as a linear operator mapping from the domain of the deformation gradient to the range of its transpose. Similarly, we can define the *left Cauchy-Green strain tensor* as

$$\mathbf{B}_{t_0}^{t}(\mathbf{x}_0) = \nabla \mathbf{F}_{t_0}^{t}(\mathbf{x}_0)\left[\nabla \mathbf{F}_{t_0}^{t}(\mathbf{x}_0)\right]^{\mathrm{T}}, \tag{1.5}$$

leading to a simple relation between the right and the left CG tensor

$$\left[\mathbf{C}_{t_0}^{t}\right]^{-1} = \mathbf{B}_{t}^{t_0}, \tag{1.6}$$

which clearly illustrates the correlation between the right and the left Cauchy-Green strain tensors [Haller, 2023].

The right and the left Cauchy-Green strain tensors are used in different scenarios. The right tensor is used for forward computations, whereas the left tensor is used for backward computations. Since the transition between them is denoted by the simple Relation 1.6, we will continue to only consider the right tensor, as computations for the left tensor can be very easily derived in a similar manner. Due to its definiton, the CG tensor has some important mathematical properties. It is a symmetric tensor (meaning we can easily find eigenvalues and eigenvectors) and it is positive-definite (meaning eigenvalues are positive). These properties allow further analysis and the derivation of the finite-time Lyapunov exponents (FTLE) [Haller, 2023].

1.3 Finite-time Lyapunov exponents

Let us consider a material surface $\mathcal{M}(t)$ and trajectories $\mathbf{x}(t; t_0, \mathbf{x}_0) \in \mathcal{M}(t)$. Here, the material surface can be defined using the flowmap $\mathbf{F}_{t_0}^t$ as

$$\mathcal{M}(t) = \mathbf{F}_{t_0}^t \left(\mathcal{M}(t_0)\right). \tag{1.7}$$

Similarly, infinitesimally small material perturbations $\boldsymbol{\xi}(t)$ along those trajectories can be computed using the deformation gradient $\nabla \mathbf{F}_{t_0}^t$ as

$$\boldsymbol{\xi}(t) = \nabla \mathbf{F}_{t_0}^t (x_0)\, \boldsymbol{\xi}(t_0). \tag{1.8}$$

Furthermore, the magnitude of the perturbation can be expressed using the CG tensor as follows:

$$|\boldsymbol{\xi}(t)| = \sqrt{\langle \nabla \mathbf{F}_{t_0}^t (\mathbf{x}_0)\, \boldsymbol{\xi}(t_0), \nabla \mathbf{F}_{t_0}^t (\mathbf{x}_0)\, \boldsymbol{\xi}(t_0) \rangle} = \sqrt{\langle \boldsymbol{\xi}(t_0), \mathbf{C}_{t_0}^t (\mathbf{x}_0)\, \boldsymbol{\xi}(t_0) \rangle}. \tag{1.9}$$

The braket notation used simply refers to computing the scalar product [Haller, 2023].

Taking into account the formula for finding eigenvalues λ_i of the CG tensor (and their eigenvectors $\boldsymbol{\xi}_i$)

$$\mathbf{C}_{t_0}^t \boldsymbol{\xi}_i = \lambda_i \boldsymbol{\xi}_i, \tag{1.10}$$

we easily obtain

$$|\boldsymbol{\xi}_i(t)| = \sqrt{\lambda_i}. \tag{1.11}$$

Therefore, the perturbation $\boldsymbol{\xi}$ aligning with the eigenvector $\boldsymbol{\xi}_i$ will be stretched by the factor $\sqrt{\lambda_i}$, which is (by definition) both the square root of the eigenvalue of the CG tensor and the singular value of the deformation gradient Haller [2023]. The evolution of eigenvectors in time is illustratively shown in Figure 1.4.

The exponent assosiated with the largest coefficient λ_n is then called the *finite-time Lyapunov exponent*, defined as

$$\mathrm{FTLE}_{t_0}^{t_1} (\mathbf{x}_0) = \frac{1}{2\,|t_1 - t_0|} \log \lambda_n (\mathbf{x}_0; t_0, t_1), \tag{1.12}$$

where for *forward* FTLEs we have $t_1 > t_0$ and for *backward* FTLEs we have $t_1 < t_0$. Ridges of locally largest values of FTLE define different types of LCSs. Similarly to streamlines (curves tangent to the velocity field) we can define *strainlines*, which are curves tangent to the $\boldsymbol{\xi}$-field [Haller, 2023].

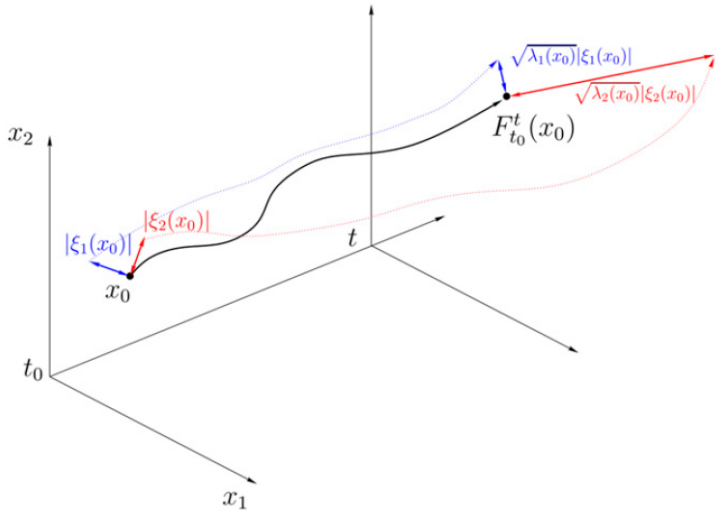

Figure 1.4: Evolution of eigenvectors. Eigenvectors $\boldsymbol{\xi}_1(x_0)$, $\boldsymbol{\xi}_2(x_0)$ evolve in time t via flowmap $F^t_{t_0}(x_0)$ and eigenvalues $\lambda_1(x_0)$, $\lambda_2(x_0)$. [Serra et al., 2017]

1.4 Lagrangian coherent structures

Computation of FTLEs produces LCSs which allow for deep analysis of fluid dynamics. Let us remind the definition of LCSs given by Haller [2023] at the beginning of this chapter: "Lagrangian coherent structures (LCSs) are codimension-1, structurally stable material surfaces that locally extremize attraction, repulsion or shear among all nearby material surfaces over a finite time interval $[t_0; t_1]$". We can now specify different types of LCSs [Haller, 2023].

Attracting LCSs are denoted by the largest values of backward FTLEs. They are often readily identifiable as visible accumulation of tracers accompanies them. *Repelling LCSs* are denoted by the largest values of forward FTLEs. They play an important role in identifying masses of fluid that do not intermix over a specific time interval. Attracting and repelling LCSs are colectively referred to as *hyperbolic LCSs* [Haller, 2023].

Apart from hyperbolic LCSs we can also define *elliptic* and *parabolic LCSs*. These structures are significant in terms of shear, in other words the tangential shift of adjacent paths. Elliptic LCSs are material surfaces which are locally most shearing. Similarly, parabolic LCSs are material surfaces which are locally least shearing [Haller, 2023].

A visualisation of hyperbolic LCSs is shown in Figure 1.5. Streamlines (a) represent the velocity field given, hyperbolic LCSs (b) are computed from the velocity field. Another example is seen in Figure 1.6. We can see the evolution of a material parcel over the time interval $[t_0, t_1]$ and the corresponding hyperbolic LCSs. Lastly, in Figure 1.7 we see comparison of hyperbolic LCSs in 2D and 3D.

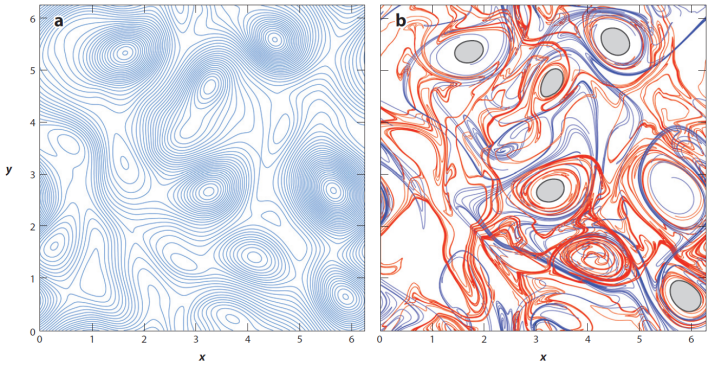

Figure 1.5: Visualisation of streamlines and hyperbolic LCSs. (a) streamlines of a chosen velocity field (blue), (b) corresponding strainlines: attracting LCSs (red), repelling LCSs (blue). [Haller, 2015]

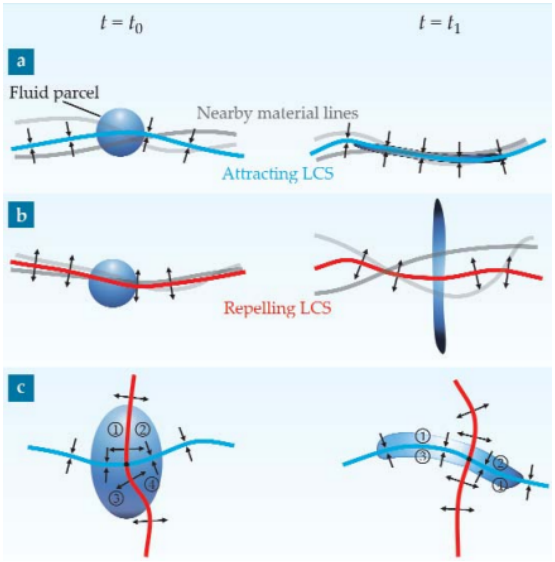

Figure 1.6: Deformation of a fluid parcel. (a) attracting LCSs (blue) and stretching of the parcel, (b) repelling LCSs (red) and shrinking of the parcel, (c) both attracting and repelling LCSs. [Peacock and Haller, 2013]

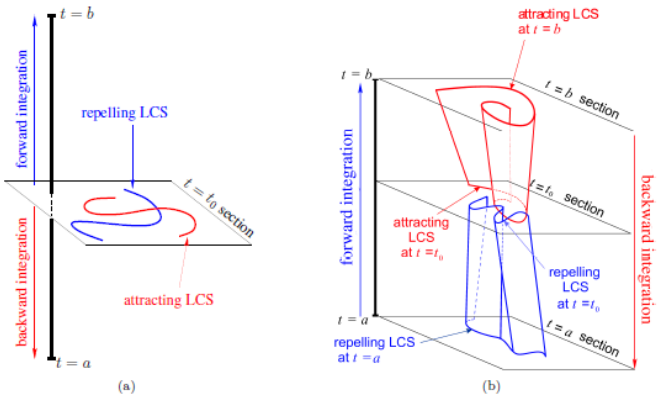

Figure 1.7: Comparison od hyperbolic LCSs in 2D and 3D. Repelling LCSs (blue) and attracting LCSs (red) are computed at different times. (a) 2D (b) 3D. [Farazmand and Haller, 2013]

2. Stratospheric winter polar circulation

The stratospheric winter polar circulation is often referred to as simply the *polar vortex*. However, this term also defines a different phenomenon, that is the circulation in the troposphere, as seen in Figure 2.1. It is therefore important to distinguish those two, as they are not connected and have generally different properties, e.g. the tropospheric polar vortex is much larger and it exists all year, whereas the stratospheric polar vortex experiences seasonal changes [Waugh et al., 2017]. In this thesis, we will use the term polar vortex when referencing the stratopheric circulation. The term stratosphere refers to the atmospheric layer that resides above troposphere, approximately between 6 to 50 km above sea level (depending on latitude) [Mohanakumar, 2008].

2.1 The structure of the polar vortex

The polar vortex is marked by westerly winds in the stratosphere, stretching from the pole to up to 30° latitudes, with the largest winds at approximately 60° latitudes [Waugh et al., 2017].

The polar vortex generally consists of two major regions. That is the *main vortex* and the *surf zone*, separated by the *vortex edge*. The main vortex is a coherent rotating mass of cold air, whereas the surf zone is widely incoherent and it extends into lower latitudes and interacts with warmer air [Serra et al., 2017]. Visualisation of the structure of the polar vortex can be seen in Figure 2.2.

Polar vortex exists both on the Northern Hemisphere (NH) and the Southern Hemisphere (SH). However, despite their seeming similarities, their properties differ. With much more diverse topography and great upward waves, the NH generates more unstable vortex than its southern counterpart.

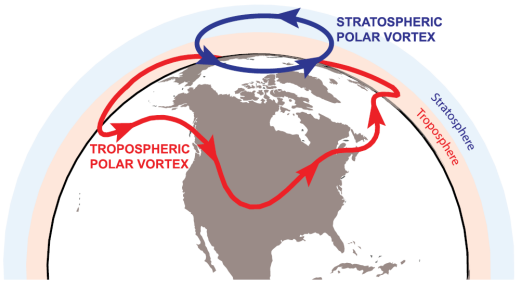

Figure 2.1: Stratospheric and tropospheric polar vortex. The stratospheric vortex (blue) is smaller and located at higher altitudes than the tropospheric vortex (red). [Waugh et al., 2017]

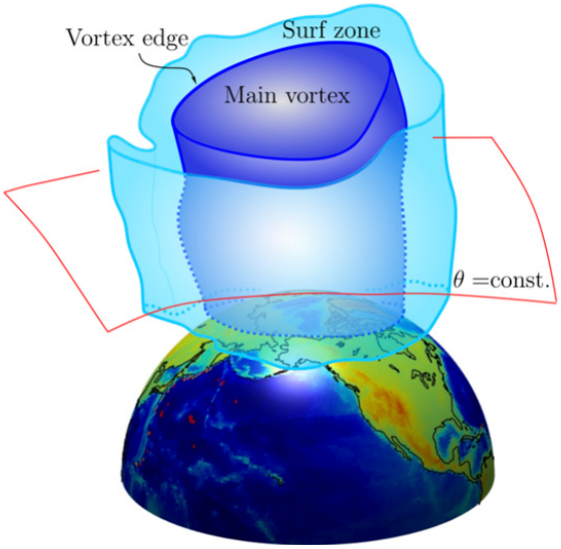

Figure 2.2: Structure of the polar vortex. The main vortex (dark blue), vortex edge, the surf zone (light blue), isentropic surface (red). [Serra et al., 2017]

2.2 Relevance of the polar vortex

As previously mentioned, the properties of the NH and SH polar vortices are not the same. This leads to differences in their relevance. The SH polar vortex in highly significant regarding the formation of the ozone hole, whereas the NH polar vortex strongly influences surface weather. Let us briefly introduce those two phenomena.

The ozone layer is a part of the stratospehere protecting the lower atmosphere from ultraviolet radiation (UV). The UV radiation poses as a huge threat to human health, as it can cause various types of diseases, skin cancer being the most prominent. Unfortunately, there has been evident depletion of the ozone layer, the most significant manifestation of which is known as the *ozone hole*. The ozone hole occurs in the Antarctic region, where low ozone concentrations closely match the extent of the polar vortex [Zhang et al., 2017]. Significance of the NH polar vortex lies in different aspects. Its stability is vital to the winter surface weather, as its collapse can lead to extreme weather events impacting the regions of North America, northern Europe and Asia [Thompson et al., 2002]. The event in question is called *sudden stratospheric warming* (*SSW*). With the breakdown of the polar vortex, a huge mass of cold air is released, potentially creating extreme changes in the surface weather. On NH, SSW occurs approximately every two years. Therefore, determining the edge of the polar vortex and its changes can provide useful information regarding predictions of those extreme weather patterns [Serra et al., 2017].

An example from history is studied in Overland et al. [2020]. In 2018, the event of SSW brought an extreme amount of snow to Eurasia. It was dubbed the "Beast from East". Another example of the SSW-effects is visible though the study of the impacts on vegetation, as in [Li et al., 2017], which focuses on boreal Eurasia from 1982 to 2015.

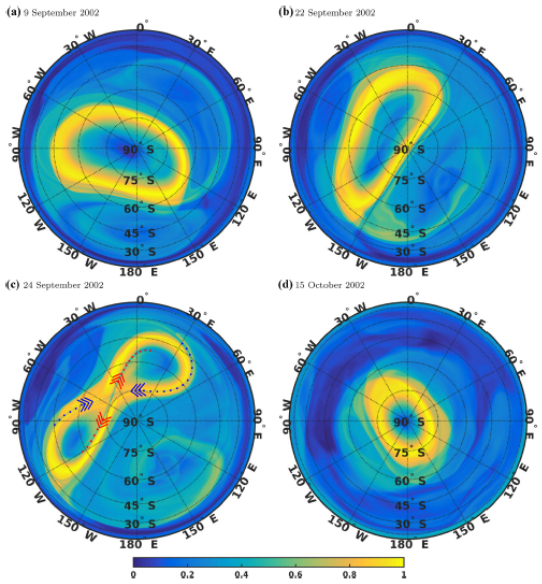

Figure 2.3: Splitting of polar vortex in 2002 on SH. Visualisation of the polar vortex on the Southern Hemisphere with visible split in (c), also showing stable (blue) and unstable (red) manifolds. [Curbelo et al., 2019]

2.3 Seasonal changes of the NH polar vortex

In this thesis, our focus is on the NH polar vortex. Let us now describe its seasonal changes (including the SSW events).

With the start of winter, polar regions with polar night experience rapid coolings, creating a gradient of temperatures between polar and tropical regions. As a result, wind velocities in the stratosphere also increase. Due to the Coriolis effect and the spin of the Earth, a counterclockwise rotating motion is created with dominant westerly winds [Serra et al., 2017, Waugh et al., 2017].

When the vortex becomes unstable it collapses, freeing a mass of cool air that descends to lower altitudes while rising polar temperatures. The breakdown typically occurs mid-winter. Ridges, mountains and other surface discontinuities create different areas of waves which, if strong enough, can cause changes in the polar vortex. These waves are called the *Rossby waves*. The vortex can either completely cease to exist, or smaller daughter vortices can be created. Usually, there are two centers of the daughter vorticies, located in Siberia and North America [Serra et al., 2017]. Splitting into two daughter vortices during a unique event of SSW on SH in 2002 is visualized on Figure 2.3.

2.4 Methods of detecting the polar vortex

Successfully detecting the edge of the polar vortex has been a challenge for many decades now. Eulerian diagnostic methods have been used in the past, with the rise of Lagrangian methods [Serra et al., 2017].

A fairly popular Eulerian method works with the distribution of potential vorticity (PV). The boundary of the vortex edge is detected as the isoline of the maximum gradient of PV. Shortcomings of this method are that it is frame

dependent and nonmaterial [Nash et al., 1996, Serra et al., 2017].

Another PV-based method for uncovering the edge focuses on finding the PV isoline with minimal material stretching over a specific time interval. This approach is more general than the one introduced by Nash et al. [1996] as it is material. However, the frame dependency is still viable [Serra et al., 2017]. For its properties, this method is called "semi-Lagrangian" Chen [1994].

Visualising the edge of the polar vortex can be determined also by studying the concentration of ozone. As discussed earlier, ozone hole strongly corresponds to the formation of the polar vortex, with low concentrations in its center. Similarly, we can look at the temperature field, which shows low temperatures in the center. With both those methods, Lagrangian approaches using material structures (such as LCSs) show remarkable compatibility [Serra et al., 2017]. Visualisation of some of the methods discussed can be seen in Figure 2.4.

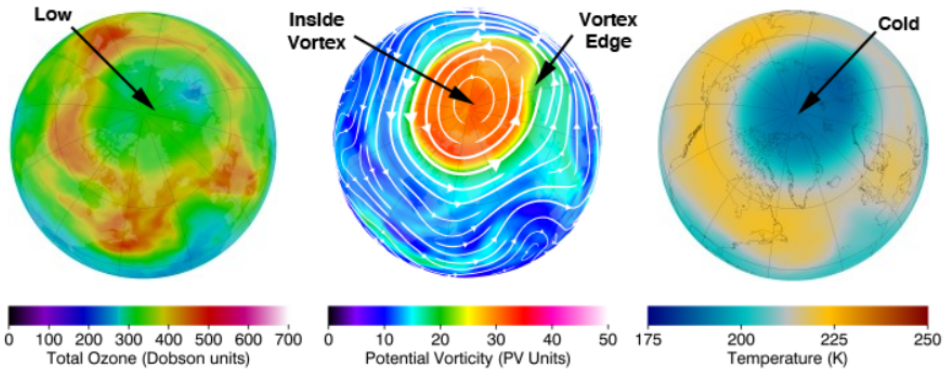

(a) NH

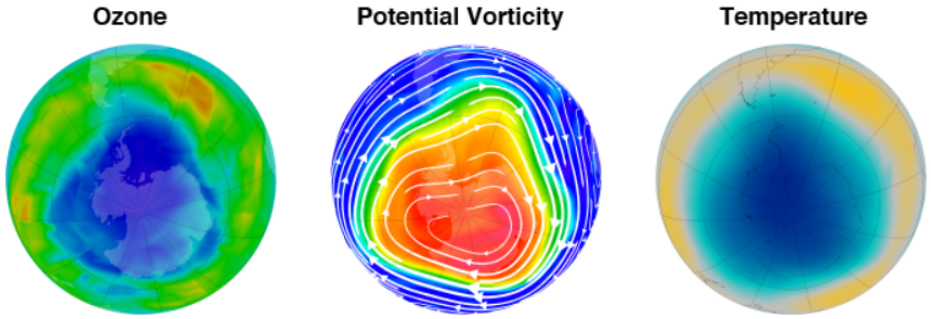

(b) SH

Figure 2.4: Different methods of detecting vortex boundary. Ozone, PV and temperature methods. PV on the 460 K level, temperature on the 50 hPa level. (a) NH, February 22, 2011 (b) SH, August 22, 2011. [[NAS]]

3. Application of LCSs on atmospheric data

In this chapter, we apply the theory covered in previous chapters. Given a velocity field around the North Pole, we attempt to implement the computation of Lagrangian coherent structures and analyse the results in order to study the changes of the circulation. Many programs for computing LCSs exist in the programming language MATLAB, however, our computations are conducted in Python.

3.1 Data

Initially, we tried to analyse ERA5 hourly data [ERA]. However, our computations never yielded any satisfactory results. Later we discovered that the data provided are static and do not evolve in time. This finding led us to search for a better set of data that would generate correct velocity field. The data that proved satisfactory and are used for our final computations are MERRA2 [ERA](Modern-Era Retrospective analysis for Research and Applications, Version 2).

We look at the wind velocity $\mathbf{u} = (u, v)$, where u denotes zonal winds and v denotes meridional winds. Our set of data focuses on the winter period December 2007 to February 2008 using 3-hourly data in netCDF format. The polar region studied covers the area of latitudes from 30 °N to 90 °N for all longitudes. We subsequently look at four pressure levels: 20 hPa, 10 hPa, 5 hPa and 1 hPa.

3.2 The velocity field

Before any computations leading to the LCSs, we can examine the magnitudes of the components of wind (the u- and v-components) for different times and different pressure-levels. First, let us compare the u- and v-components. In Figure 3.1 we look at data at 10 hPa for December 01, 2007, January 19, 2008 and February 27, 2008. These time slots were chosen randomly for simple illustration. We can see that the westerly winds are highly predominant. Specially, on January 19, 2008 we can distinctively see a fully formed polar vortex. Although the v-components are significant for computing LCSs, their visualisation does not give us any additional information. For that, we will further restrict ourselves to only visualising the u-components of wind.

As stated, data for January 19, 2008 show a formed circulation. The early days of February, 2008 show similar velocity field (Figure 3.2). Stable polar vortex is distinctly recognizable. We can see it rotate, however, there are not visible any great changes in shape. Zonal winds reach up to over 100 m/s.

Another approach to visualise our data is to look at different pressure levels. To further examine the stable polar circulation we look at February 03, 2008 (Figure 3.3). Comparing the velocity fields at 20 hPa, 10 hPa, 5 hPa and 1 hPa, we can see that the vortex slightly rotates and decreases in size as it stretches to

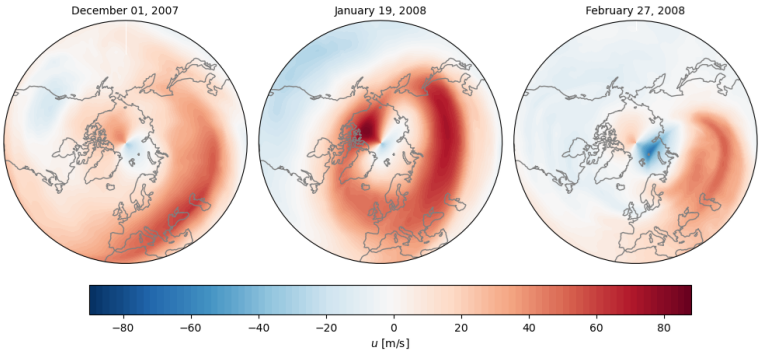

(a)

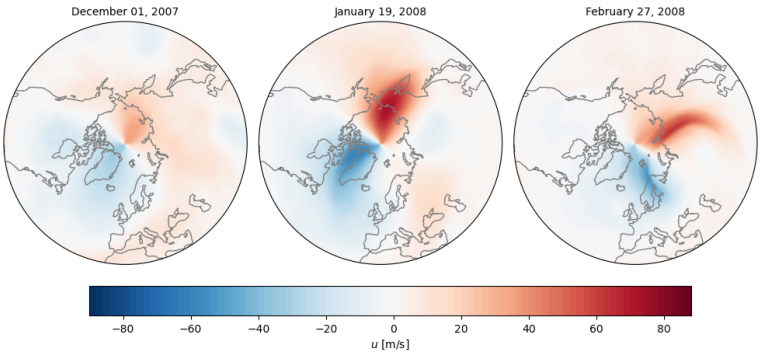

(b)

Figure 3.1: Comparison of the u- and v-components of wind at 10 hPa. (a) u- (b) v-components of wind for December 01, 2007, January 19, 2008 and February 27, 2008

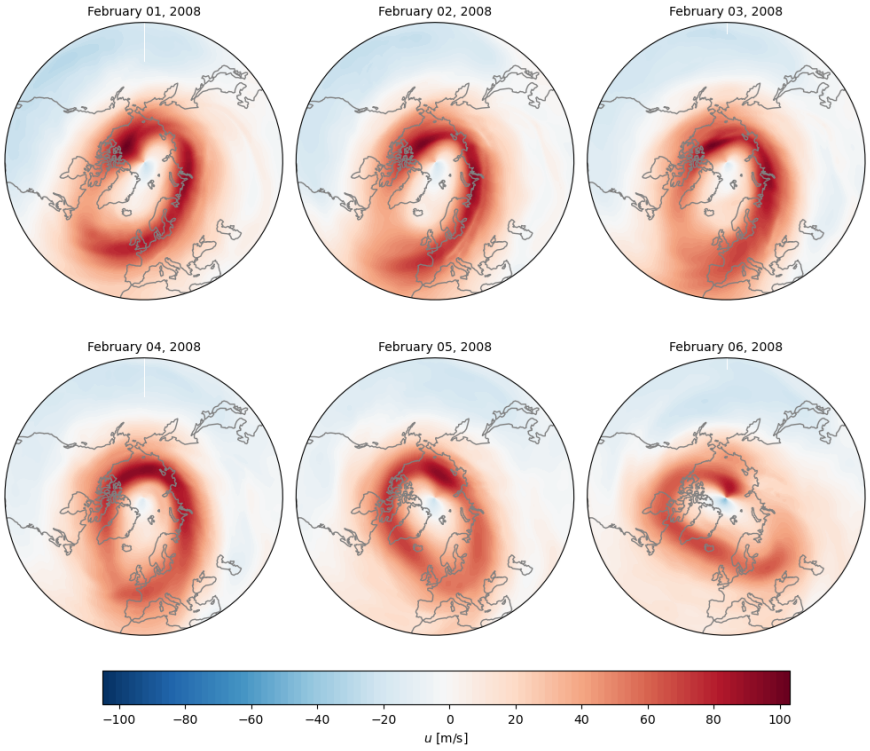

Figure 3.2: The u-components of wind at 10 hPa. Evolution over February 01, 02, 03, 04, 05 and 06, 2008.

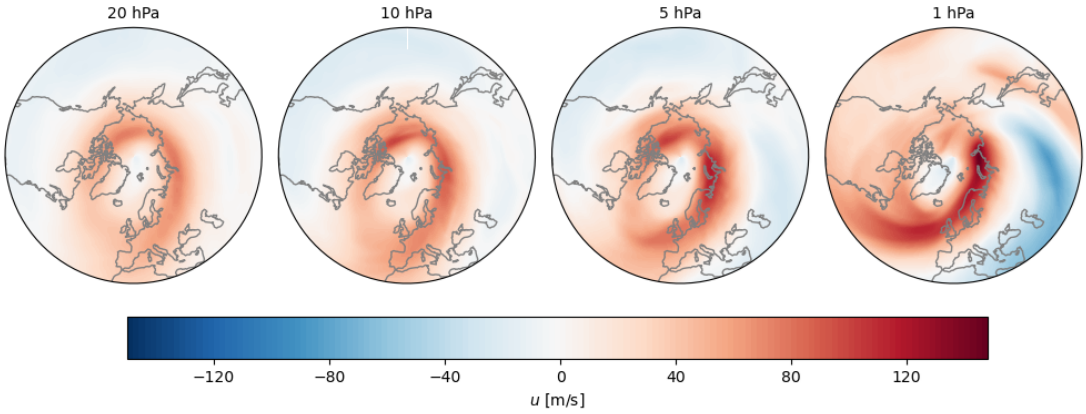

Figure 3.3: The u-components of wind at different pressure levels. Computation for 20 hPa, 10 hPa, 5 hPa and 1 hPa on February 03, 2008.

higher altitudes, with more distinguished shape at lower altitudes. However, for lower pressure levels, velocities highly increase, with maximum velocities up to almost 140 m/s.

3.3 The program

For our computations we used the Python programming language. Haller [2023] provides a Python script for calculating different types of transport barriers, including hyperbolic LCSs, which will be the focus of our research. However, the script provided must be modified, as there are several major disparities between the code given and the essential properties of our data. The initial program takes in a small amount of data and interpolates it over a rectangular meshgrid. Since we look at a large polar region, the code must be adjusted so that it can

- take large-scale high resolution data,
- convert velocities from units m/s to deg/3h,
- interpolate over a spherical grid,
- compute over the pole without any singularity.

3.4 The RK4 method

Before we give a detailed description of our computations we must first introduce the numerical method used for calculating trajectories from velocity field. The method used is called the *Fourth Order Runge-Kutta* (*RK4*). We will not go into much detail, as examining numerical solutions is not the main purpose of this thesis. We will only explain the main principles.

Let us consider a differential equation with an initial condition

$$\dot{\mathbf{x}}(t) = \mathbf{v}(t, \mathbf{x}), \quad \mathbf{x}(t_0) = \mathbf{x_0}. \tag{3.1}$$

Choosing a stepsize h, such that $t_{n+1} = t_n + h$, we obtain iteration

$$\mathbf{x_{n+1}} = \mathbf{x_n} + h\dot{\mathbf{x}}. \tag{3.2}$$

Using the Taylor series, we can rewrite the expression as

$$\mathbf{x_{n+1}} = \mathbf{x_n} + h\sum_{i=1}^{q} \omega_i \mathbf{k_i}, \tag{3.3}$$

where ω_i and k_i are specific coefficients from the Taylor series. Clearly, the higher q, the higher the precision of the computation. This approach is called the *Runge-Kutta method* [Süli and Mayers, 2003].

A specific selection $q = 4$ gives a simplified form

$$\mathbf{x_{n+1}} = \mathbf{x_n} + \frac{h}{6}\left(\mathbf{k_1} + 2\mathbf{k_2} + 2\mathbf{k_3} + \mathbf{k_4}\right), \tag{3.4}$$

where

$$\mathbf{k_1} = \mathbf{v}\left(t_n, \mathbf{x_n}\right), \tag{3.5}$$

$$\mathbf{k_2} = \mathbf{v}(t_n + \frac{1}{2}h, \mathbf{x_n} + \frac{1}{2}h\mathbf{k_1}), \tag{3.6}$$

$$\mathbf{k_3} = \mathbf{v}(t_n + \frac{1}{2}h, \mathbf{x_n} + \frac{1}{2}h\mathbf{k_2}), \tag{3.7}$$

$$\mathbf{k_4} = \mathbf{v}\left(t_n + h, \mathbf{x_n} + h\mathbf{k_3}\right). \tag{3.8}$$

This approach, using $q = 4$, is called the Fourth Order Runge-Kutta method. Using this method, trajectories (and subsequently the flowmap) can be easily computed from the given velocity field [Süli and Mayers, 2003]. The visualisation of RK4 can be seen in Figure 3.4.

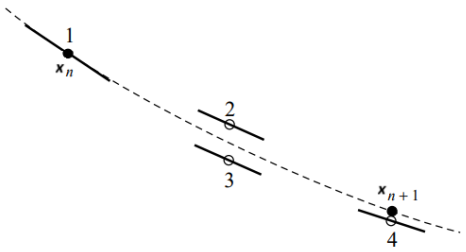

Figure 3.4: Visualisation of the RK4 method. Four computed derivatives of $\mathbf{x_n}$ (dots 1, 2, 3 and 4) leading to the expected position of $\mathbf{x_{n+1}}$. Trajectory is shown using a dashed line. [Teukolsky et al., 1992]

With an established method to compute trajectories, we can now further explore the code, highlight the problems we encountered throughout and follow the computation process covered in Chapter 1.

3.5 The trajectories

The aim of this section is to succesfully apply the RK4 method introduced in Section 3.4 and generate a flowmap. The steps required are:

1. define data on a grid (time, longitude, latutide, u-component of wind, v-component of wind),
2. interpolate data,
3. use the RK4 method for
    - a specific set of ICs (used for calculating one specific trajectory) or
    - all possible ICs (used for calculating LCSs).

We are given the following data:

- velocity field u, where $[u] = \mathrm{m/s}$,
- velicity field v, where $[v] = \mathrm{m/s}$,
- longitude coordinates x, where $[x] = °$,
- latitude coordinates y, where $[y] = °$,
- time t, where $[t] = 3\mathrm{h}$.

First, we need to correctly transform the data so that they satisfy our computations. The code is as follows.

```
import numpy as np

def convert_velocity(x,y,u,v,pressure,data_height):

    y_co = 90 - y
    x_rad, y_rad = np.radians(x), np.radians(y_co)
    X, Y = np.meshgrid(x_rad,y_rad)

    u_rad3h, v_rad3h = x_rad.copy(), y_rad.copy()

    pressure_level = [20,10,5,1]
    position = np.where(pressure_level == pressure)
    p = position[0][0]
    H = data_height[:,p,:,:]

    # Radius of the Earth in m
    R = 6370 * 1000

    for i in range(X.shape[0]):
        for j in range(Y.shape[1]):
            u_rad3h[:,i,j] = (u[:,i,j]/(np.cos(Y[i,j])*(R+H[:,i,j])))*3600*3
            v_rad3h[:,i,j] = (v[:,i,j]/(R+H[:,i,j]))*3600*3

    return u_rad3h, v_rad3h

U, V = convert_velocity(x,y,u,v,pressure,data_height)
```

We first transform our coordinates to radians (the reason for will be explained later). Variables `u` and `v` are our given velocity fields in the shape `np.shape(u), np.shape(v) = (Nt, Ny, Nx)`, where `Nt, Ny, Nx` denote the number of `t, y, x` inputs. Transition from cartesian to spherical coordinates is rather complicated, as we are given pressure levels, not above sea levels. This problem is fixed by introducing an additional set of data (also MERRA2), that will provide the height for each point on our meshgrid. We call them `data_height`. Lastly, we choose a specific pressure level we want to examine and we acquire **u** in the units of rad/3h.

The next step is the interpolation of data. Here, we encounter a rather complex problem as the North Pole acts as a singularity. The script provided by Haller [2023] does not work with poles, therefore further adjustments must be done. One possible solution could be shifting the singularity from pole to the equator - an

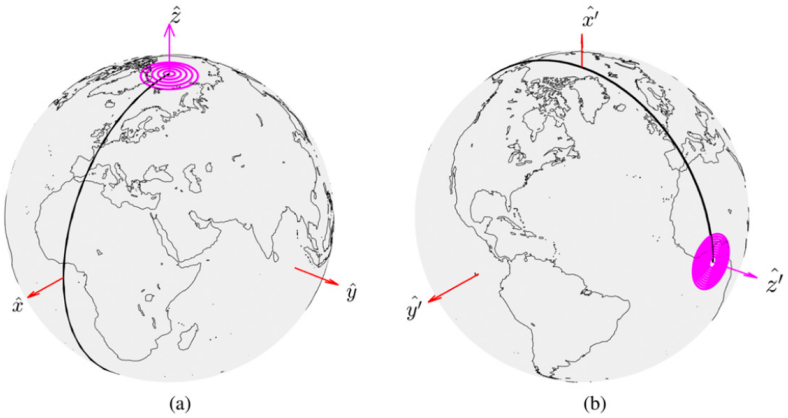

Figure 3.5: Shifting singularity from the pole to the equator. (a) original coordinate system (b) new coordinate system [Serra et al., 2017]

approach introduced by Serra et al. [2017]. The study focused on finding LCSs around the North Pole with computations carried via MATLAB. The idea behind shifting the pole is visualised on Figure 3.5. Unfortunately, we could not overcome this modelling problem using Python. Despite hours of work, this part of the code remains unresolved. As a result, further computations of trajectories are not appropriately corresponding to the velocity field studied. However, there is still potential to calculate LCSs and examine our results, even if the initial computation of trajectories is slightly different from the actual trajectories.

Before we continue with the computations of trajectories, let us briefly display the relevance of computing LCSs from our inexact trajectories on Figure 3.6. The figure shows a trajectory from February 01, 2008 to February 03, 2008 and corresponding computed repelling LCSs. We can see that the LCS acts as a barrier which the particle following the computed trajectory does not cross. Regarding repelling LCSs, that is the exact result we would expect. We will cover the computations of LCSs in more detail in Section 3.6.

Let us return to the interpolation. In the original script, interpolation is performed over a rectangular grid. Clearly, our spherical area requires a more complex solution. We use spherical interpolation `RectSphereBivariateSpline` from the library `scipy.interpolate`. This function requires a meshgrid of coordinates in radians, thus explaining our former need to transform velocities from degrees to radians. It also requires the input of colatitudes rather then latitudes. The code reads as follows.

```
from scipy.interpolate import RectSphereBivariateSpline as RSBS
import numpy as np

def interpolant_sphere(x,y,U,V):

    y_co = 90 - y
    x_rad, y_rad = np.radians(x), np.radians(y_co)
    X, Y = np.meshgrid(x_rad, y_rad)

    Interpolant = [[], []]

    for j in range(U.shape[0]):

        Interpolant[0].append(RSBS(Y[:,0],X[0,:],U[j,:,:]))
        Interpolant[1].append(RSBS(Y[:,0],X[0,:],V[j,:,:]))

    return Interpolant

Interpolant = interpolant_sphere(X,Y,U,V)

Interpolant_u = Interpolant[0]
Interpolant_v = Interpolant[1]
```

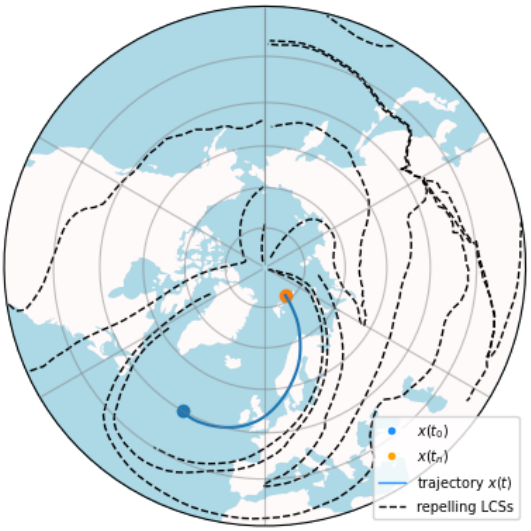

Figure 3.6: Comparison of trajectory and repelling LCSs. Computed trajectory from February 01, 2008 to February 03, 2008 with corresponding computed repelling LCSs.

We tried to dispose of the singularity using the `RectSphereBivariateSpline` function, as it is promoted as one of the properties of the function (see [RSB]). However, the problem with singularity was not resolved and it continues to be a major resctriction regarding our analysis. It is the best approximation we were able to obtain for interpolation of large-scale high resolution data on a sphere.

The interpolation is then used for finding the exact values of velocities at specific time- and space-positions, which is incorporated into the RK4 numerical method. Obtained trajectories create a flowmap, from which we compute the LCSs. We can show the Python script for the computation using the RK4 method below.

```
import numpy as np

def velocity(t,x,Interpolant_u,Interpolant_v):

    for i in range(x.shape[1]):
        if x[1,i] < 0:
            x[1,i] = -x[1,i]
            x[0,i] = np.pi - x[0,i]

    k = int(t)

    u = Interpolant_u[k](x[1,:],x[0,:],grid = False)
    v = Interpolant_v[k](x[1,:],x[0,:],grid = False)

    vel = np.array([u,v])

    return vel

def RK4(t, x, dt, Interpolant_u, Interpolant_v):

    k1_0 = velocity(t,x,Interpolant_u,Interpolant_v)[0]
    k2_0 = velocity(t + .5*dt,x + .5 * dt * k1_0,Interpolant_u,Interpolant_v)[0]
    k3_0 = velocity(t + .5*dt,x + .5 * dt * k2_0,Interpolant_u,Interpolant_v)[0]
    k4_0 = velocity(t + dt,x + dt * k3_0,Interpolant_u,Interpolant_v)[0]

    k1_1 = - velocity(t,x,Interpolant_u,Interpolant_v)[1]
    k2_1 = - velocity(t + .5*dt,x + .5 * dt * k1_1,Interpolant_u,Interpolant_v)[1]
    k3_1 = - velocity(t + .5*dt,x + .5 * dt * k2_1,Interpolant_u,Interpolant_v)[1]
    k4_1 = - velocity(t + dt,x + dt * k3_1,Interpolant_u,Interpolant_v)[1]

    x_update_u = x[0] + dt * (k1_0 + 2 * k2_0 + 2 * k3_0 + k4_0) / 6
    x_update_v = x[1] + dt * (k1_1 + 2 * k2_1 + 2 * k3_1 + k4_1) / 6

    x_update = np.array([x_update_u,x_update_v]).reshape(2,-1)
```

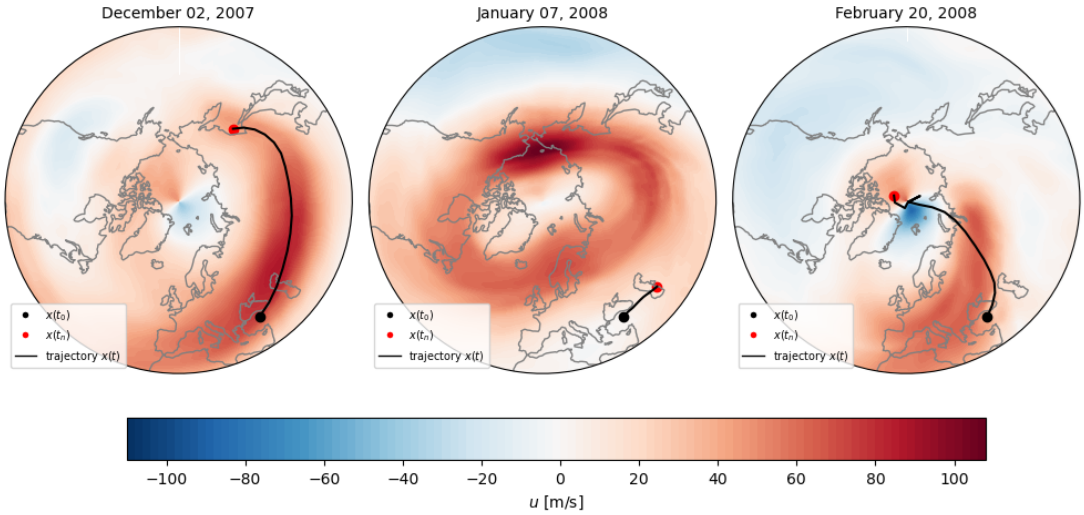

Figure 3.7: Examples of computed trajectories. Computed trajectories at 10 hPa for December 02, 2007, January 07, 2008 and February 20, 2008. Initial position 35 °E, 40 °N. In the background, u-component of wind.

```
return x_update
```

The code has two specifics that need further clarification. First, in the `velocity` function we can see that we must be careful when computing negative colatitudes. The program itself, as previously stated, is not optimal around the pole. From the structure of the grid, we can see that the instance of negative colatitudes is in fact a positive value of colatitude with the appropriate longitude being complementary to π. The second fact we should address is that in the `RK4` function, for positions in the y-direction (meaning using the v-component of wind), we take negative values of velocities. That is due to the fact that our coordinates changed from latitudes to colatitudes. Lastly, we provide some examples of computed trajectories, as seen in Figure 3.7. We can see that on December 02, 2007 the trajectory very clearly corresponds with the velocity field, as it moves with a part of the polar vortex. On January 07, 2008, we see a clearly formed polar vortex, however, the trajectory computed is outside the main vortex, likely in the surf zone, where the velocities are not as high.

Lastly, on February 20, 2008 we see the behaviour of a trajectory around the North Pole not exactly reflecting the velocity field. As discussed earlier, the pole does set restrictions to our computations. Nevertheless, we see that our process for computing trajectories is satisfactory, even with its limitations.

3.6 The LCSs

The rest of the computations does not require many significant changes to the original code provided by Haller [2023]. The algorithm follows the mathematical foundations covered in Chapter 1. However, there are some variables that need to be determined. That is

- the step size for integration,
- the threshold distance to locate local maxima,

- the maximum length of a strainline,
- the number of relevant strainlines,
- the minimum threshold on rate of attraction of a strainline,
- the threshold number of iterations.

We set those values as (in the same order): 0.05, 0.5, 5, 20, 0, 100.

Using the program, we inspect three events: the formation, stabilization and collapse of the polar vortex. We compute LCSs over a period of four days for pressure levels 20 hPa, 10 hPa, 5 hPa and 1 hPa. Visualisation of the velocity field along with the corresponding LCSs is in Figures 3.8, 3.10 and 3.12. Further computations showing LCSs over subsequent time periods can be seen in Figures 3.9, 3.11 and 3.13. We will analyse those results in Chapter 4.

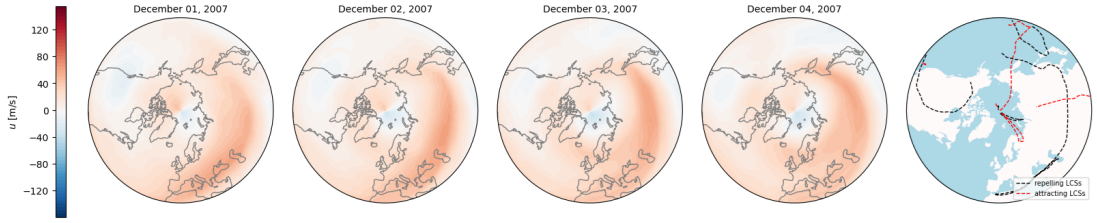

(a) 20 hPa

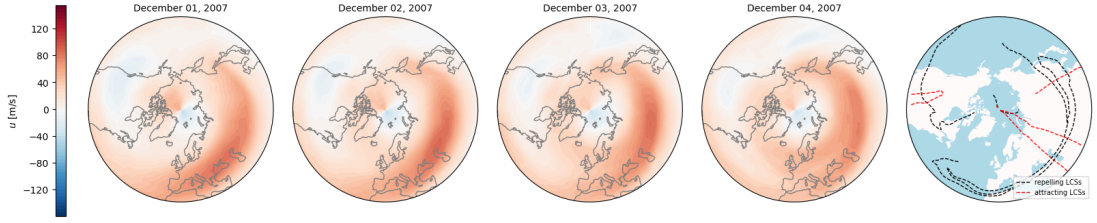

(b) 10 hPa

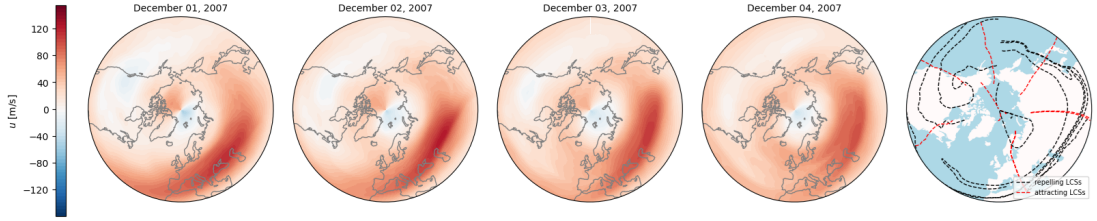

(c) 5 hPa

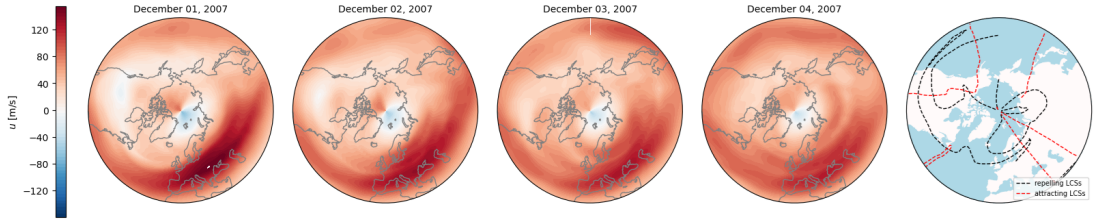

(d) 1 hPa

Figure 3.8: Formation of the polar vortex. The u-component of wind for December 01, 02, 03 and 04, 2007 with corresponding repelling and attracting LCSs computed during the same time frame. Computations for pressure levels (a) 20 hPa, (b) 10 hPa, (c) 5 hPa, (d) 1 hPa.

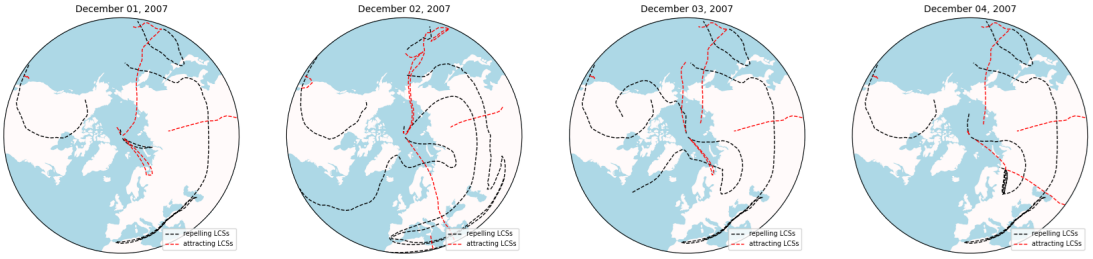

(a) 20 hPa

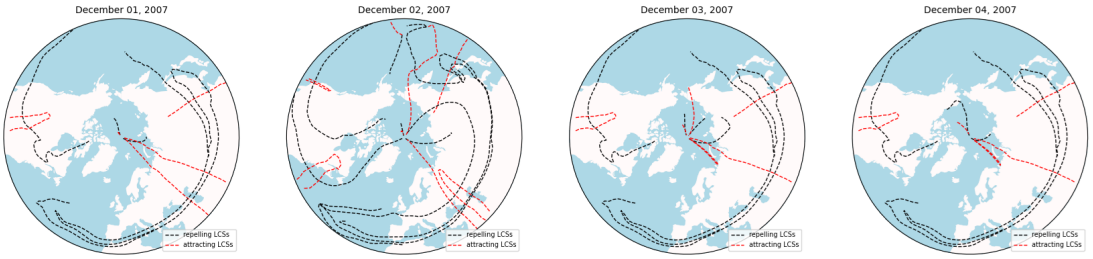

(b) 10 hPa

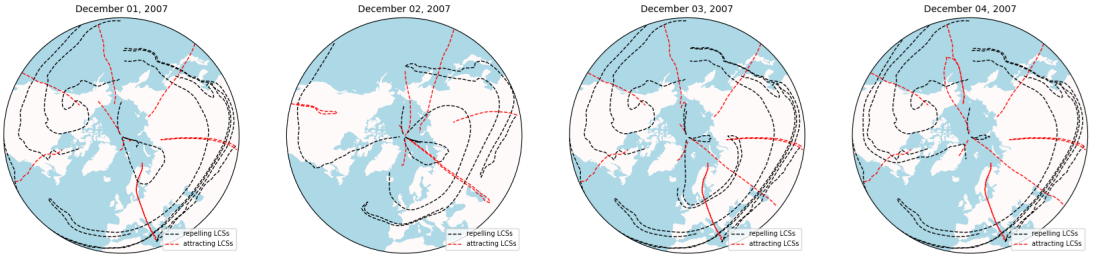

(c) 5 hPa

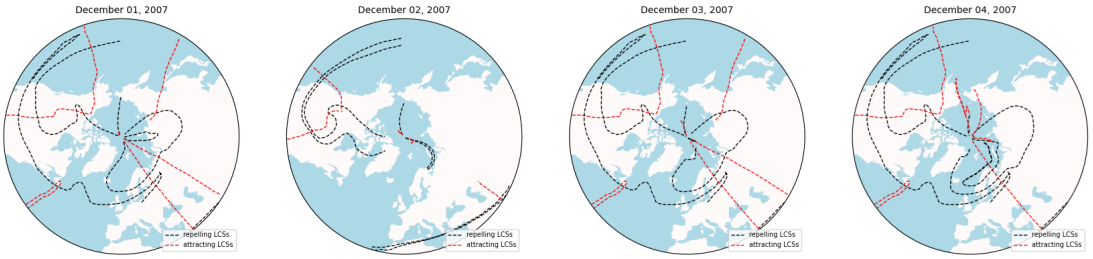

(d) 1 hPa

Figure 3.9: LCSs for the formation of the polar vortex. Computed repelling (black) and attracting (red) LCSs over a period of four days. Time stamp above each computation denotes the starting point for each computation: December 01, 02, 03 and 04, 2007. Data for four pressure levels are shown (a) 20 hPa, (b) 10 hPa, (c) 5 hPa, (d) 1 hPa.

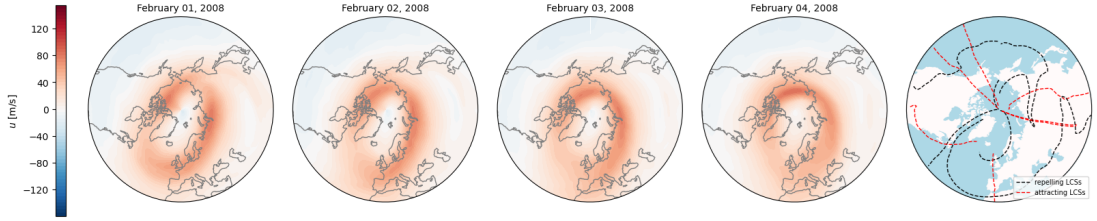

(a) 20 hPa

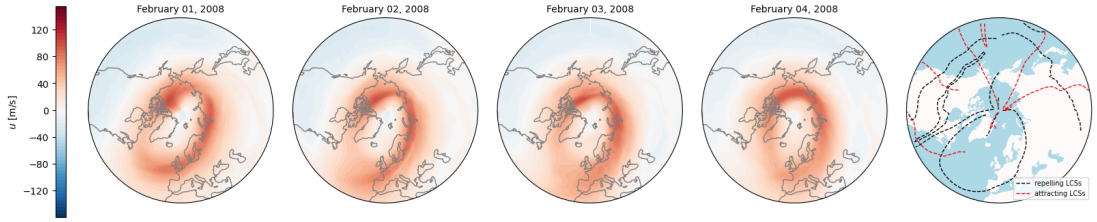

(b) 10 hPa

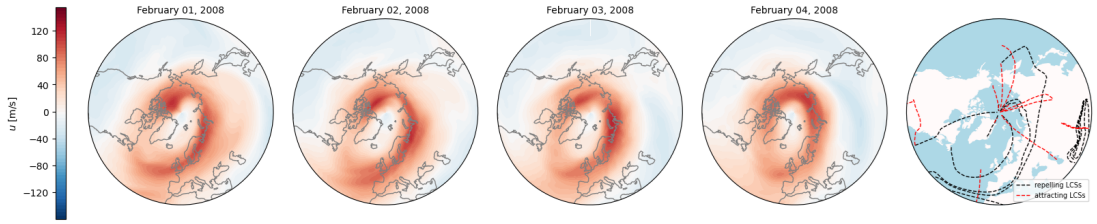

(c) 5 hPa

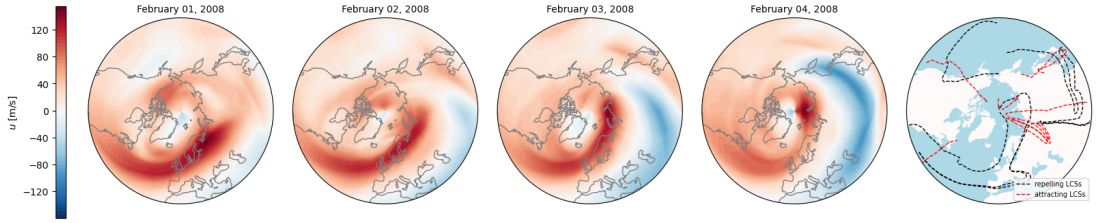

(d) 1 hPa

Figure 3.10: Stable circulation. The u-component of wind for February 01, 02, 03 and 04, 2008 with corresponding repelling and attracting LCSs computed during the same time frame. Computations for pressure levels (a) 20 hPa, (b) 10 hPa, (c) 5 hPa, (d) 1 hPa.

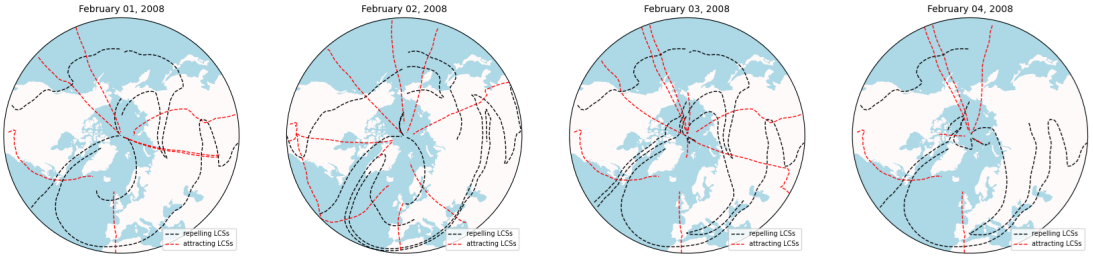

(a) 20 hPa

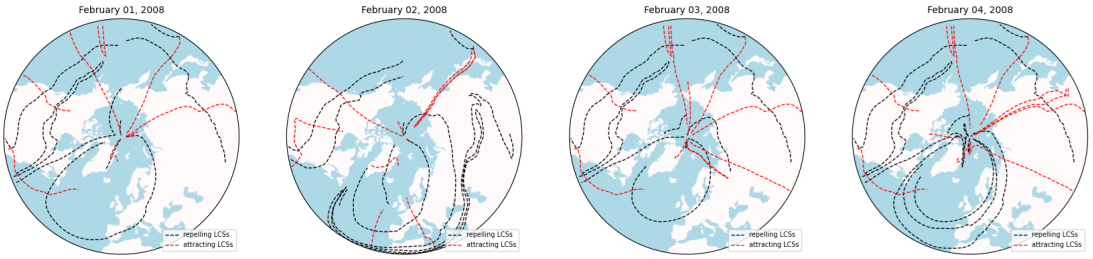

(b) 10 hPa

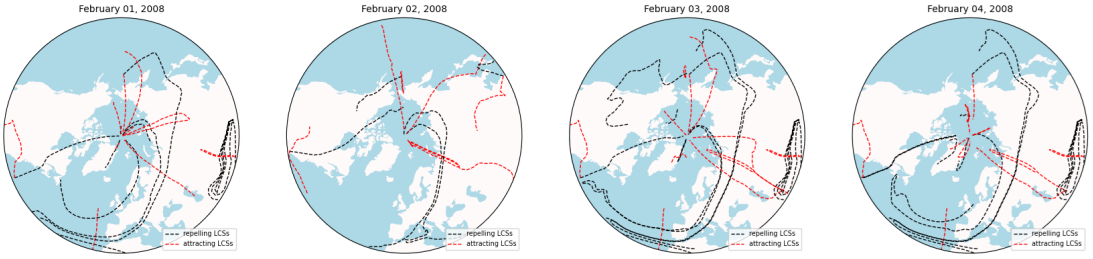

(c) 5 hPa

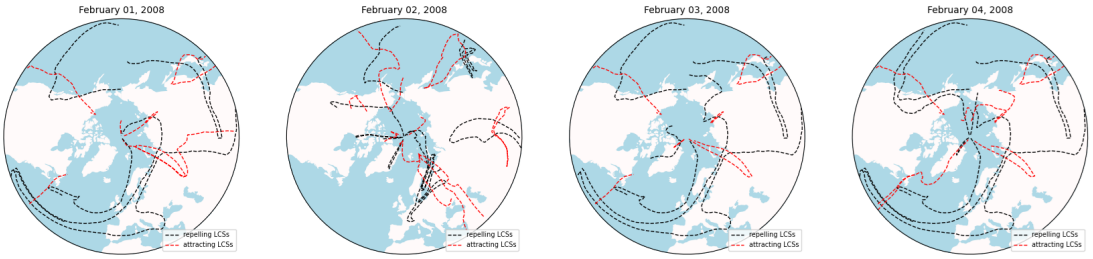

(d) 1 hPa

Figure 3.11: LCSs for stable circulation. Computed repelling (black) and attracting (red) LCSs over a period of four days. Time stamp above each computation denotes the starting point for each computation: February 01, 02, 03 and 04, 2008. Data for four pressure levels are shown (a) 20 hPa, (b) 10 hPa, (c) 5 hPa, (d) 1 hPa.

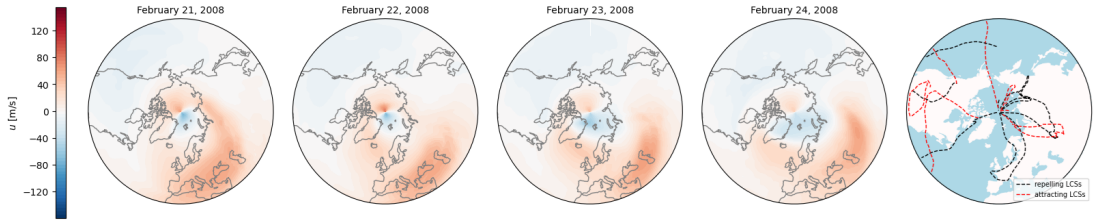

(a) 20 hPa

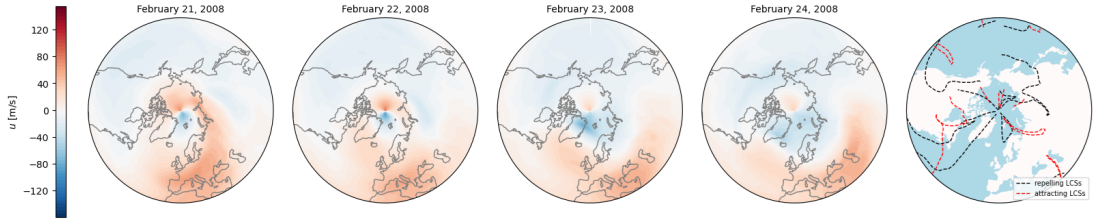

(b) 10 hPa

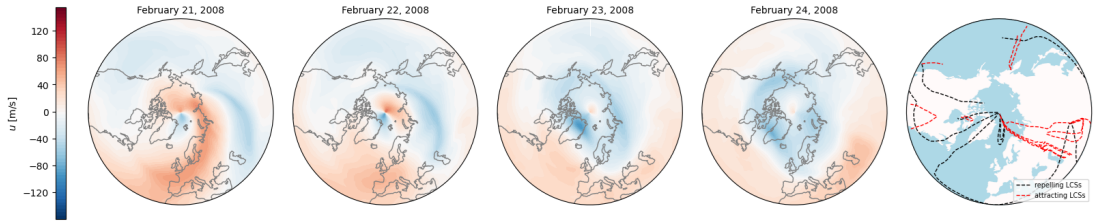

(c) 5 hPa

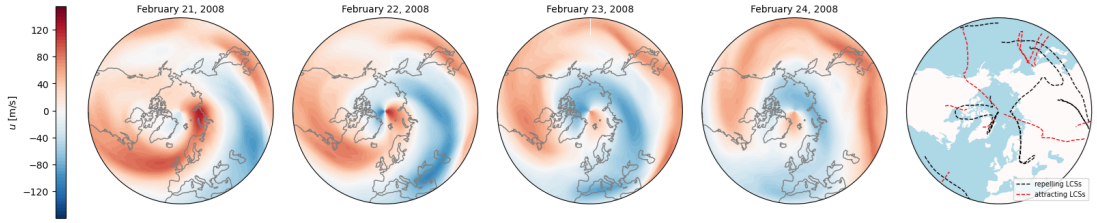

(d) 1 hPa

Figure 3.12: Collapse of the polar vortex. The u-component of wind for February 21, 22, 23 and 24, 2008 with corresponding repelling and attracting LCSs computed during the same time frame. Computations for pressure levels (a) 20 hPa, (b) 10 hPa, (c) 5 hPa, (d) 1 hPa.

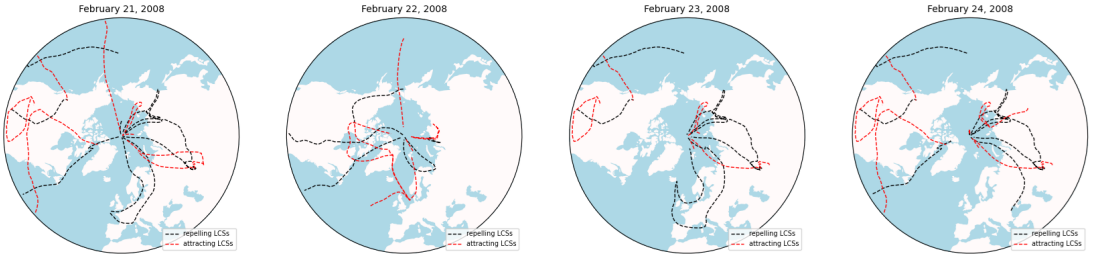

(a) 20 hPa

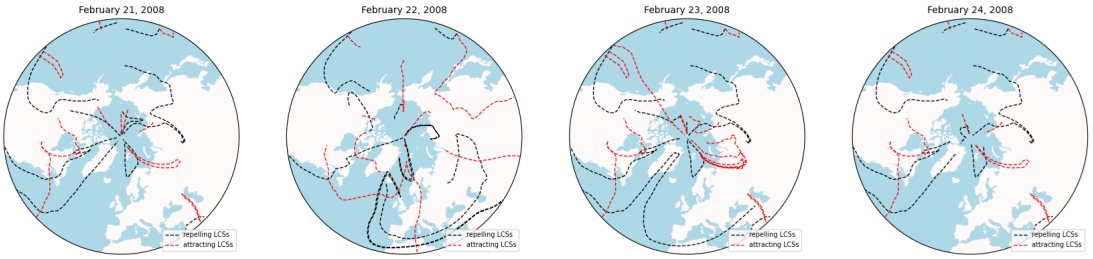

(b) 10 hPa

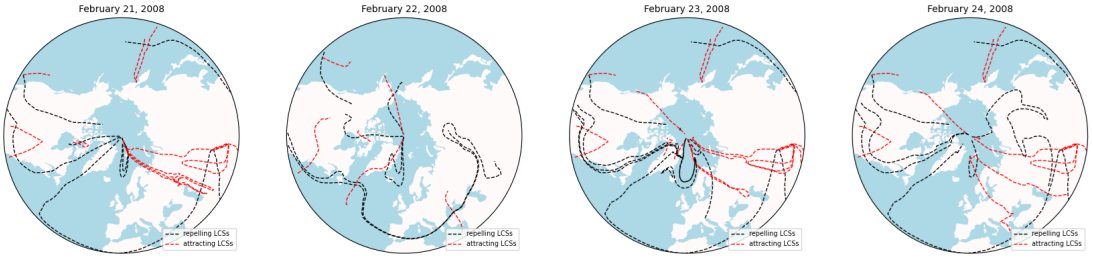

(c) 5 hPa

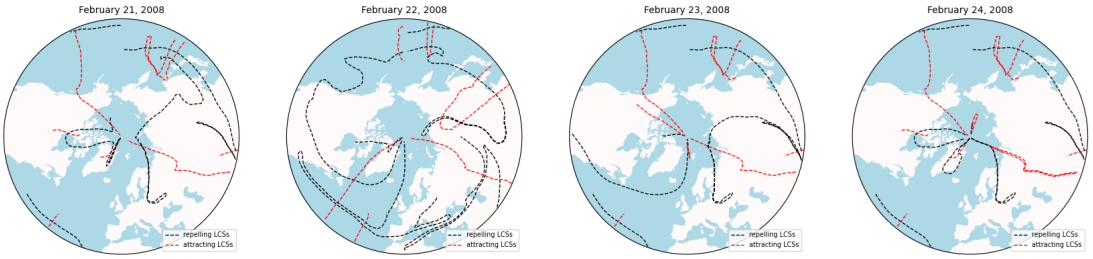

(d) 1 hPa

Figure 3.13: LCSs for the collapse of the polar vortex. Computed repelling (black) and attracting (red) LCSs over a period of four days. Time stamp above each computation denotes the starting point for each computation: February 21, 22, 23 and 24, 2008. Data for four pressure levels are shown (a) 20 hPa, (b) 10 hPa, (c) 5 hPa, (d) 1 hPa.

4. Analysis of results

In Section 3.6 we performed several computations of hyperbolic LCS on atmospheric data for winter 2007/2008. In this chapter, we study the results in detail and analyze their interpretations. We ran computations for three different time periods with the efforts of capturing the formation, stabilization and collapse of the polar vortex. Repelling LCSs (black) should give us the boundary of the vortex, whereas the attracting LCSs (red) should show the area of biggest material accumulation over a selected time period.

4.1 Formation of the polar vortex

The first computation we carried was for the time period of the early days of December 2007 (Figure 3.8). We can see the beginning of formation of the vortex. First, let us examine the velocity field. With lower pressure levels we can see increase in the magnitude of zonal winds. That is, the maximum the u-component achieves at 20 hPa lies around 40 m/s, whereas for higher altitudes, such those at 1 hPa, it increases up to over 120 m/s. However, we can clearly see the circular movement throughout the whole span of pressure levels. Computed repelling LCSs resemble a U-shape, uncovering a detectable circular motion. Looking at Figure 3.8c and Figure 3.8d, we can even spot closed curves, indicating a stable circulation. Thus we can determine that in higher altitudes (Figure 3.8c, Figure 3.8d), the circulation has somewhat stabilized, whereas in the lower altitudes (Figure 3.8a, Figure 3.8b), there is a circular pattern visible (especially in the first quater), however, there are no closed curves visible.

Computations of LCSs over subsequent days in Figure 3.9 give further insight. The calculations were also carrier over the duration of four days with differentiating starting days. The differences between the lower and higher altitudes are very illustrative. First, let us analyze the pressure level 1 hPa (Figure 3.9d). For each time stamp, with the exclusion of December 02, 2007, we can see a prominent oval shape at the pole, signaling a stable structure. This gives us a definite conclusion, that during those four days, the circulation at 1 hPa was coherent. The exception of December 02, 2007 can be caused by either wrong computations (e.g. singularity at pole, small number of chosen relevant strainlines,...) or some abnormalities in the flow that would temporaly influence the coherence of the material boundary. In Figure 3.9c the formation of the vortex is visible. There is no exact apparent pattern, however, there are noticible circular shapes. At different times, those shapes are either close or unclosed, indicating the complex evolution of the vortex. For lower altitudes seen in Figure 3.9a and Figure 3.9b there are no closed shapes visible, with a persisting U-shape in the first quater.

The attrating LCSs calculated do not give us any additional information regarding the boundary of the vortex. Examining all results in Figure 3.8 we can say that they are most present in the first and second quater which corresponds with the highest magnitudes of the u-velocity.

The analysis of Figure 3.8 and Figure 3.9 shows that at lower pressure levels, the circulation was already somewhat stable, whereas at higher pressures the stabilisation is yet to occur. Such conclusions could not be obtained from

only visualisating the velocity field. Here, the repelling LCSs show promising results regarding the different behaviour of air mass at different pressures in the stratosphere.

4.2 Stable circulation

Let us show an example of stable circulation in the winter of 2007/2008. After browsing through different time periods, we found a fitting illustation for the first four days of February, 2008. Following the same format as in Section 4.1, we now discuss the results seen in Figure 3.10 and Figure 3.11.

In Figure 3.10 the velocity field shows a clear image of a stable vortex. A particularly intresting is the comparison of different pressure levels. The vortex seems to be changing its tilt with altitude. This is an interesting observation, showing that the vortex is not a well defined cylinder, but rather a cylinder-like spiraling object. With respect to time, we can highlight the fact that the shape of the vortex does not significantly change, although it does slightly alter its direction. Nevertheless, the circulation itself seems to be stable.

Examining the results shown in Figure 3.11 will give us a better insight into the stability of the vortex in question. The best results for a stable vortex are seen for higher pressure levels 20 hPa and 10 hPa in Figure 3.11a and Figure 3.11b. We would expect closed circular-like curves represented by the repelling LCSs that do not change significantly in time. At 20 hPa, we see a trend of a closed area in the lower half of the polar plot. We better understand this trend when we look at 10 hPa. Here, there are visible closed structures great in size, clearly indicating a coherent structure. From those results the conclusion of a stable circulation is only fitting. In Figure 3.11c there is a similar trend in the shape of the repelling LCSs as in Figure 3.11a. In Figure 3.11d, however, there is no circulation visible. Nonetheless, we do see very similar structures for all four days with a slight exception of the results for February 02, 2008.

Attracing LCSs do not show any particular significance. There does not seem to be any specific tendency concerning their shape. The only consistent pattern is their pole-ward orientation.

After the previous analysis of our results regarding stable circulation of the polar vortex, we can conclude the following. Using the method of repelling LCSs, the polar vortex is seen to be stable at the beginning of February, 2008 around the 10 hPa level. For both lower and higher pressure levels, its coherence decreases, more predominantly for the lower levels. At 1 hPa, there seems to be no apparent circulation, although coherent movement is detected.

4.3 Collapse of the polar vortex

The last part of our analysis concerns the collapse of the polar vortex. Ideally, evident SSW would be detected. This was the trickiest part of our computations, as even after a long search for clear sightings, we could not, with high certainty, observe an undefiable event of SSW. We ran several computations. Splitting of the vortex was not detected. We did manage to detect a collapsed vortex. However, no clear event of the ongoing breakdown of the vortex was found. The

best results (here, best means *best illustrative*) were given for the time period of February 21 to February 24, 2008. We show the results in Figures 3.12 and 3.13.

Figure 3.12 shows the remains of the polar vortex in the lower altitudes (Figures 3.12a and 3.12b), whereas in the higher altitudes the polar vortex is not detectable at all. Specifically, we can see reverse directions of the zonal winds, indicating major changes in the circulation. Computed LCSs are shown in detail in Figure 3.13. For lower altitutudes, we see a few closed curves, although not circular in shape. Especially in Figure 3.13a we see a trend of two closed curves, suggesting splitting into two daughter vortices. However, the visualised velocity field does not support this hypothesis. It is possible that this computation was highly affected by the singularity at pole, thus showing not conclusive results. Results shown in Figures 3.13b and 3.13c show hints of circular motion, however there seems to be any significant structure. In Figure 3.13d we see chaotic curves, from which we cannot draw any definite conclusions.

The attracting LCSs show highly different behaviour in comparison with Figures 3.9 and 3.11. Their shapes are irregular, they no longer have a distinctive direction to the pole. This finding can support our observation of not coherent flow around the North Pole.

Thus, the stratospheric motion during the time period February 21 to February 24, 2008, shows a collapsed vortex, with no indications of coherent flow in the higher altitudes. In the lower altitudes, there are some remains. This time period therefore experiences the disintegration of the polar vortex. However, the results are not very distinctive.

5. Discussion

In this chapter, we discuss the strengths and shortcomings of our computations and introduce possible improvements for future research.

5.1 The program

The premise of this thesis was jeopardized at its beginning with the realisation that there are no accessible Python programs that would be suitable for the study of the polar vortex. We were faced with an unexpected task, that is to find and successfully rewrite a code that somewhat satisfies our conditions. This task was not entirely successful, as explained in Chapter 3. The singularity at pole was the biggest obstacle we encountered. Nevertheless, we decided to show our results despite its faults. Therefore, it is important to keep in mind that our results are impaired by inaccurate computations of trajectories from a given velocity field.

These hardships could be bypassed or resolved by using different techniques. There are accessible scripts written in the MATLAB programming language. If further examined, these programs could eventually solve the singularity problem using approaches we did not discover. In our calculations, we used the RK4 method. As this thesis is not numerical based, we did not attempt to find other numerical solutions. There could be more accurate approaches to determine the flowmap from a velocity field. However, examining them would require a deeper understanding of mathematical modelling that highly surpasses the objective of this thesis. Lastly, the problem itself could be possibly resolved at its root by changing the coordinate system, as briefly mentioned in Chapter 3. This is the approach we investigated, unfortunately to no competent outcomes. Further research could lead to potentially fixing the problem at hand.

5.2 The data

Obtaining sufficient data was met with struggles as well, leading to unnecessary weeks of work until the discovery that the ERA5 data had been corrupted from the beginning. As a result, we opted to use MERRA2 data instead, which proved to give expected results regarding the velocity field around the North Pole during winter months. Our data set contained time periods with the step size of 3 hours. To gain more precise results, we could apply data sets with the step size of 1 hour, which are generally accessible by ERA5 (had it not been corrupted).

The velocity field with which we ran our computations was in the units of m/s. To interpolate over our grid, which was in spherical coordinates, we needed to transform metres to radians. We did so using the radius of the Earth set as R = 6370 m. We took this constant from the original program provided by Haller [2023]. Better results could be obtained from adjusting the constant with reference to the position on the longitude-latitude grid.

5.3 The results

We decided to show the visualisation of the u-components of the wind, rather than showing the v-components, or even both. To show the v-component as well was thought redundant, as the main flow occurs in the x-direction. However, to show both of the components could provide a better understanding of the velocity field. The judgement to visualise one component using a colour meshgrid rather than visualising both the u- and v-components using arrows as vectors was done as a result of highly detailed grid. Our efforts to pleasantly visualise using arrows were met with no great success.

In Section 3.6 we state the inputs of our variables regarding the computations of LCSs. We tried to optimize the outputs for our data, where we ran computations for various different values and determined the final values based on observation. We kept the values of the variables set throughout all calculations. It is possible that different threshold numbers would yield different results, significant to our analysis. A possible extension of our paper could see the examination of the results given for different variable inputs and their mutual comparison, thus providing us with the opportunity for deeper analysis.

The computation of the LCSs was also affected by subjectivity as the structures are dependent on the chosen time frame for which they are studied. For our analysis we chose to compute for the time interval spanning over four days. After running many test calculations, we determined it to be the best time frame, yielding both appropriate results and being sufficient to visualise and interpret. A viable extension of this paper could be to investigate different lengths of time intervals and compare the results.

For our analysis, we chose three specific events in the winter of 2007/2008. To apply the LCSs for the whole time period provided by our data set would be inessential and possibly confusing, as the aim of this paper is to demonstrate the application of the LCSs qualitevly, not quantitevly. Nevertheless, our results are restrained to only three events. To evaluate LCSs at many other time periods could present another possible extension of this paper. Additionaly, comparisons of the same time periods during the winter season but in different years could be an interesting insight into the yearly changes of the vortex.

We ran computations only for hyperbolic LCSs, as that was the main aim of this thesis. It could be intriguing to additionally compute elliptic and/or parabolic LCSs and compare the results, thus finding the best method for determining the boundary of the vortex. For visualising the velocity field, extra data such as e.g. the ozone concentration could be also provided and compared.

5.4 The analysis

Our analysis was based purely on observations and our interpretation of the LCSs over a polar grid. Our conclusions were drawn by examining the shape of the strainlines. There, repelling LCSs showed as the most valuable in the search for the vortex edge. Attracting LCSs served as a secondary source of information, as they also showed a certain type of coherence over the specified time period.

We examined three events. The formation and the stabilisation of the vortex were fairly conclusive, allowing us to draw satisfactory deductions from our

computations, even with their shortcomings regarding the singularity at pole.

The collapse of the vortex was also detected, although the actual disintegration of the vortex would need better computations. We cannot state the exact time period of the SSW. This restriction is likely in our program, rather than in the method LCSs provide. It is also possible that in the winter 2007/2008 there was no abrupt case of SSW. We can only speculate where the biggest malfunction of our program lies but can definitely argue that solving the singularity problem would eliminate the largest obstacle this thesis faced. It is most likely that only after would we receive much better results.

5.5 Further insights

Although our results have their shortcomings, the illustation of the possible advantages of using the hyperbolic LSCs regarding the polar vortex was sufficiently examined. Even with slightly disturbed flowmap, we received qualitevly important results, once again demonstrating the potential the LCS-method introduces.

Had we been provided with functional program for computing, this thesis would indulge in a more thorough examination of the polar vortex, with possibilites stated in the previous sections of this chapter. However, as no applicable program was available, we were faced with a challenge to optimize and rewrite an unsuitable program provided by Haller [2023]. This optimalization took months, but we can safely say, that our efforts were not in vain, as we provide and analyse results that nonetheless carry value to the study of the polar vortex.

Conclusion

In this thesis, we introduced the topic of Lagrangian coherent structures and demonstrated this method on atmospheric data of winter 2007/2008.

In Chapter 1 we explained the construction of LCSs, focusing on both the mathematical and the physical aspect. We described the computation of LCSs, different types of LCSs and their significance.

In Chapter 2, we gave a characterization of the polar vortex, defining its variations (stratospheric, tropospheric, northern and southern). We aimed our focus on the stratospheric polar winter circulation on the Northern Hemisphere, examining its seasonal changes. We also discussed different techniques and the importance of detecting the edge of the polar vortex.

In Chapter 3 we showed the process of our computations, describing the difficulties regarding programming in the Python language. We detailed the parts of our program that needed adjusting and discussed the problems encountered, the main one being the singularity at pole. That was an issue we could not, even after numerous attempts, resolve. We also introduced a numerical method RK4 used for deriving trajectories from a velocity field.

We further illustrated the velocity field, giving its examples at different pressure levels and different times. Finally, we ran our computations to find hyperbolic LCSs. We opted for showing three distinctive events in the winter period: the formation, the stabilisation and the collapse of the vortex. All computations were performed for pressure levels 20 hPa, 10 hPa, 5 hPa and 1 hPa and calculated for the duration of four days.

In Chapter 4 we analysed the results from Chapter 3. We were able to detect the behaviour of the polar vortex at the event of its formation and stabilization. A collapsed polar vortex was observed, however, the results were not persuasive, as in this part of the computations, it is likely that the singularity at pole was significant. A clear event of SSW was not found.

In Chapter 5 we explained the shortcomings of our computations and possible improvements for the future. We also stated that, despite its challenges, out aim to demonstrate the application of hyperbolic LCSs on the stratospheric polar winter circulation was successful.

Lagrangian coherent structures remain a powerful tool for characterizing fluid dynamics. Their prospects of possible applications are vast, with a large amount of opportunities for further research. Their significance in detecting the edge of the polar vortex seems to be non-negligible. The complexity of their computation remained to be an obstacle in this thesis, however, further endeavors could provide more precise outcomes.

Bibliography

ERA5 hourly data on single levels from 1940 to present. https://cds.climate.copernicus.eu/cdsapp#!/dataset/reanalysis-era5-single-levels?tab=overview. Accessed: 2024-07-17.

NASA Ozone Watch. https://ozonewatch.gsfc.nasa.gov/facts/vortex_NH.html. Accessed: 2024-07-17.

SciPy API: Interpolation: scipy.interpolate.RectSphereBivariateSpline. https://docs.scipy.org/doc/scipy/reference/generated/scipy.interpolate.RectSphereBivariateSpline.html. Accessed: 2024-07-14.

G. Boffetta, G. Lacorata, G. Redaelli, and A. Vulpiani. Detecting barriers to transport: a review of different techniques. *Physica D: Nonlinear Phenomena*, 159(1–2):58–70, November 2001. ISSN 0167-2789. doi: 10.1016/s0167-2789(01)00330-x.

Ping Chen. *Journal of Geophysical Research: Atmospheres*, 99(D10):20563–20571, October 1994. ISSN 0148-0227. doi: 10.1029/94jd01754.

Jezabel Curbelo, Carlos R. Mechoso, Ana M. Mancho, and Stephen Wiggins. Lagrangian study of the final warming in the southern stratosphere during 2002: Part ii. 3d structure. *Climate Dynamics*, 53(3–4):1277–1286, June 2019. ISSN 1432-0894. doi: 10.1007/s00382-019-04833-x.

Mohammad Farazmand and George Haller. Attracting and repelling lagrangian coherent structures from a single computation. *Chaos: An Interdisciplinary Journal of Nonlinear Science*, 23(2), April 2013. ISSN 1089-7682. doi: 10.1063/1.4800210.

G. Haller and G. Yuan. Lagrangian coherent structures and mixing in two-dimensional turbulence. *Physica D: Nonlinear Phenomena*, 147(3–4):352–370, December 2000. ISSN 0167-2789. doi: 10.1016/s0167-2789(00)00142-1.

George Haller. Lagrangian coherent structures. *Annual Review of Fluid Mechanics*, 47(1):137–162, January 2015. ISSN 1545-4479. doi: 10.1146/annurev-fluid-010313-141322.

George Haller. *Transport Barriers and Coherent Structures in Flow Data: Advective, Diffusive, Stochastic and Active Methods*. Cambridge University Press, February 2023. ISBN 9781009225175. doi: 10.1017/9781009225199.

Jing Li, Ke Fan, Jianjun Xu, Alfred M Powell, and Felix Kogan. The effect of preceding wintertime arctic polar vortex on springtime ndvi patterns in boreal eurasia, 1982–2015. *Climate Dynamics*, 49:23–35, 2017.

K. Mohanakumar. *Stratosphere Troposphere Interactions*. Springer Netherlands, 2008. ISBN 9781402082177. doi: 10.1007/978-1-4020-8217-7.

Eric R. Nash, Paul A. Newman, Joan E. Rosenfield, and Mark R. Schoeberl. An objective determination of the polar vortex using ertel's potential vorticity. *Journal of Geophysical Research: Atmospheres*, 101(D5):9471–9478, April 1996. ISSN 0148-0227. doi: 10.1029/96jd00066.

James Overland, Richard Hall, Edward Hanna, Alexey Karpechko, Timo Vihma, Muyin Wang, and Xiangdong Zhang. The polar vortex and extreme weather: li2017. *Atmosphere*, 11(6), 2020.

Thomas Peacock and George Haller. Lagrangian coherent structures: The hidden skeleton of fluid flows. *Physics Today*, 66(2):41–47, January 2013. ISSN 1945-0699. doi: 10.1063/pt.3.1886.

Mattia Serra, Pratik Sathe, Francisco Beron-Vera, and George Haller. Uncovering the edge of the polar vortex. *Journal of the Atmospheric Sciences*, 74(11):3871–3885, 2017.

Endre Süli and David F. Mayers. *An Introduction to Numerical Analysis*. Cambridge University Press, August 2003. ISBN 9780521810265. doi: 10.1017/cbo9780511801181.

Saul A Teukolsky, Brian P Flannery, WH Press, and W Vetterling. Numerical recipes in c. *SMR*, 693(1):59–70, 1992.

David WJ Thompson, Mark P Baldwin, and John M Wallace. Stratospheric connection to northern hemisphere wintertime weather: Implications for prediction. *Journal of Climate*, 15(12):1421–1428, 2002.

Darryn W. Waugh, Adam H. Sobel, and Lorenzo M. Polvani. What is the polar vortex and how does it influence weather? *Bulletin of the American Meteorological Society*, 98(1):37–44, January 2017. ISSN 1520-0477. doi: 10.1175/bams-d-15-00212.1.

Yu Zhang, Jing Li, and Libo Zhou. The relationship between polar vortex and ozone depletion in the antarctic stratosphere during the period 1979–2016. *Advances in Meteorology*, 2017:1–12, 2017. ISSN 1687-9317. doi: 10.1155/2017/3078079.

List of Figures